Research Square

Preprints are preliminary reports that have not undergone peer review.
They should not be considered conclusive, used to inform clinical practice,
or referenced by the media as validated information.

Dual-beam scrolling interference pattern flow cytometry for high-throughput characterization of submicron sized particles Main article

Carl Emil Schøier Kovsted
cesk@dtu.dk

Technical University of Denmark
Jaco Botha
Technical University of Denmark
Jeppe Revall Frisvad
Technical University of Denmark
Lasse Pærgård Andersen
Technical University of Denmark
Rodolphe Marie
Technical University of Denmark
Emil Boye Kromann
University of Southern Denmark

Article

Keywords:

Posted Date: September 10th, 2026

DOI: https://doi.org/10.21203/rs.3.rs-10827673/v1

License: This work is licensed under a Creative Commons Attribution 4.0 International License.
Read Full License

Additional Declarations: Competing interest reported. J.B. and E.B.K. have applied for a patent regarding this instrument (EP application number 24163115.9). E.B.K. is the inventor and owner of another patent related to this instrument (EP 4109076 A1). All other authors declare no conflicts of interest.

Abstract

Characterization of nano- and submicron-sized particles is central to advancements in bioproduction, chemical catalysis, and life sciences, yet existing methods often compromise between throughput and sensitivity. Flow cytometry is a widely adopted high-throughput platform for particle characterization, but its application with nanoscale particles is fundamentally constrained by its original design for micrometer-sized biological cells. Here, we introduce a flow cytometry platform that uses illumination with a scrolling interference-pattern to enhance sensitivity for nanoscale particle detection and discrimination. The system enables differentiation of particle species at rates of up to 750 particles per second and detects gold nanoparticles as small as 15 nm and polystyrene particles down to 100 nm. Simulations of light scattering intensities from particles in a corresponding light field closely reproduce our experimental observations, providing insights for enhanced system configurations and applications. This work demonstrates a new approach to bringing flow cytometry into the nanoscale regime.

1. Introduction

In the last decade, interest in nanomaterials and nanoscale biology has increased in multiple fields including chemical catalysis, sensing, agriculture, environmental, food, and life sciences [1–5]. Sub-micrometer particles have particularly proven invaluable in nanomedicine as therapeutic agents used in drug delivery, biosensing, and gene editing [1, 6]. Naturally occurring, biological nanoparticles termed extracellular vesicles (EVs) are released by all living cells and play an important role as mediators of physiological and pathophysiological processes [7]. However, both the application of nanomedicines [8] and the disease diagnostics based on EVs [9] present unpredictability and ambiguity in therapeutic trials and physical/functional characterization, respectively. This is partly due to the limitations of the current methods for sensitive high-throughput characterization of particles in the sub-micrometer size range [10, 11].

Particle size distributions and concentrations are commonly characterized with dynamic light scattering (DLS) in bulk [12] and Nanoparticle Tracking Analysis (NTA) that provides single particle data [13]. Although these methods can characterize particles in the sub-micron size range (10-1000 nm), both rely on ensemble averaging of population statistics for deriving size distribution information and perform poorly on polydisperse samples [10, 13–15]. Transmission electron microscopy (TEM) is commonly used as a supplement to DLS and NTA for size characterization as it allows to distinguish extremely small (< 1 nm) features and also provides information on nanoparticle morphology [16]. However, TEM is a labor-intensive procedure with a low throughput, and results can be operator-dependent [17].

Flow cytometry (FCM) is a high-throughput method commonly used for characterization of cells and, more recently, biological nanoparticles from bio-fluids including EVs [18]. However, conventional flow cytometers lack the sensitivity to detect biological particles < 300 nm, thereby limiting their usefulness for nanoparticle characterization [11, 19]. Despite a range of improvements on FCM including illumination wavelength [20], high-sensitivity APDs [21, 22], higher NA detection objectives [23, 24], and

increased signal integration times [22, 25], high-resolution FCM still relies on a trade-off between throughput and a reduced lower detection limit [25], thus making it impractical for high-volume nanoparticle characterization.

Here, we present a proof-of-concept flow cytometer using a 10 MHz scrolling interference pattern, created by two intersecting laser beams, to illuminate nanoparticles as they traverse the interrogation zone inside a slightly tilted flow cell. Resultingly, a particle traversing the interrogation zone produces a time dependent scattering signal that oscillates with the frequency 9.4 MHz. By harnessing the well-defined temporal frequency encoded in the dynamic interference pattern, our flow cytometer uses lock-in detection of the light scatter signals, at the 9.4 MHz frequency, thereby excluding background noise and enabling detection of light scattered from 15 nm gold nanoparticles and 100 nm polystyrene at particle rates of 750 particles/s, outperforming the lower limit detection limit of more conventional illumination strategies using a static illumination profile. Aiming to further harness the well-defined and high-frequency spatial information encoded in the interference pattern, we demonstrate that the measured peak intensities and oscillating signal amplitudes created by the scrolling illumination pattern correlate with theoretically expected values for all measured particle types and sizes. Finally, by using our simulation model validated on the synthetic particles, we demonstrate theoretical system improvements that may further lower the limit of detection, potentially enabling the characterization of low-scattering biological nanoparticles (i.e., liposomes, LNPs, and EVs).

2. Materials and Methods

2.1 Materials (beads & buffers) (167 words)

The sensitivity of the system was evaluated using 15 ± 2 nm (Nanopartz, A11-15-BARE-DIH-1-10, LOT: O3073), 30 ± 2 nm (Nanopartz, A11-30-BARE-DIH-1-25, LOT: P4082), 50 ± 2 nm (Nanopartz, A11-50-BARE-DIH-1-25, LOT: P4083), 70 ± 2 nm (Nanopartz, A11-70-BARE-DIH-1-10, LOT: O3074), 125 ± 12 nm (Nanopartz, A11-125-BARE-DIH-1-10, LOT: O3075), 150 ± 14 nm (Nanopartz, A11-150-BARE-DIH-1-10, LOT: O3076), 200 ± 25 nm (Nanopartz, A11-200-BARE-DIH-1-10, LOT: O3077), and 500 ± 100 nm (Nanopartz, A11-500-BARE-DIH-1-10, LOT: O3078) gold (Au), and 100 ± 9 nm (Invitrogen, F8800, LOT: 2415718), 152 ± 5 nm (Thermo Scientific, 3150A, LOT: 257544), 200 ± 8 nm (Invitrogen, F8809, LOT: 2291694), 303 ± 6 nm (Thermo Scientific, 3300A, LOT: 261790), 401 ± 6 nm (Thermo Scientific, 3400A, LOT: 258557), and 496 ± 8 nm (Thermo Scientific, 3495A, LOT: 259421) NIST-traceable, non-fluorescent series 3000 polystyrene (PS) nanospheres. Sheath fluid consisted of de-ionized MilliQ water. Particles were diluted in MilliQ water to a concentration of 2.5×10^4 particles/µL unless stated otherwise to prevent swarm detection. MilliQ water and sterile-filtered Dulbecco's phosphate-buffered saline (DPBS; Cat. no. D8537; Merch Millipore) were additionally analyzed with our flow cytometer as a stand-alone sample to determine background noise in the system.

2.2 Flow cytometer set-up (30 words)

Detailed descriptions of the flow cytometer (optics, fluidics, and electronics) are shown in Fig. 1 and detailed further in the following sections with supporting figures found in the supplementary information.

2.2.1 Optical Setup (435 words)

The optical configuration of our flow cytometer is schematized in Fig. 1.**a**. A linearly polarized continuous-wave laser (Coherent, Genesis CX-355 STM), with a wavelength of 355 nm, is split into two beams of equal intensity and polarization as follows: The source beam is directed through a half-wave plate (HWP; Thorlabs, AHWP05M-340) and then through a polarizing beamsplitter (PBS; Thorlabs, CCM1-PBS25-355-HP/M), which reflects vertically polarized light into a first beam and transmits horizontally polarized light. The transmitted light then passes through a quarter-wave plate (QWP; Thorlabs, WPQ05M-355), converting its polarization to circular, before it is reflected back towards the same QWP and transformed into vertically polarized light, which is reflected by the PBS as a second beam. The two resulting beams are individually frequency-shifted using a pair of acousto-optic frequency shifters (AOFS1 & AOFS2; AA Opto-Electronic, MQ110-B30A3-UV), inducing shifts of 109 MHz and 119 MHz, respectively, yielding a 10 MHz difference in the first order diffractions. Each beam is then passed through a Glan-Laser polarizer (P1 & P2; Thorlabs, GLB5) to ensure high polarization purity and an optical shutter (Thorlabs, SH05) to allow selective blocking of either beam. The intensity profile for each frequency-shifted beam is shaped using a square aperture (SA1 & SA2; Owis, SP40), imaged onto the interrogation zone through a 20-fold demagnifying 4f system consisting of 400 mm (L1 & L2; Edmund Optics, #48–292) and 20 mm (L3 & L4; Thorlabs, LA4647-UV) focal length lenses. The two beams overlap in the interrogation zone inside an optofluidic flow cell (Hamamatsu, J12800-000-B5A), thus creating a scrolling interference pattern with a distinctive scrolling frequency of 10 MHz matching the relative difference between induced frequency-shifts of the two beams. The flow cell is slightly rotated around the x-axis (Fig. 1a, **inset**) to induce a small lateral movement for particles traversing the interrogation zone. The detection path consists of two conjugated 4f systems placed almost orthogonal to the incident beams. Scattered light is first magnified 14.3-fold by a 35 mm focal length collection lens (L5; Thorlabs, LA4052-UV, 0.33 Numerical Aperture (NA) in air) and a 500 mm focal length lens (L6; Thorlabs, LA4184-UV-ML). A 355/10 bandpass filter (BP; Thorlabs, FLH355-10) rejects spectral noise and stray light between L5 and L6. To reduce detection of light scattered from structures beyond the interrogation zone, a circular aperture (CA) is placed in the conjugate image plane (i.e., conjugate to the interrogation zone). A second 4f system (L7 & L8; Thorlabs, LA4148-UV) relays the collected light to a silicon photomultiplier (SiPM; Broadcom, AFBR-S4N22P014M) placed slightly off-focus from a conjugate image plane to distribute collected light more evenly across the active surface of the SiPM.

2.2.2 Fluidics Setup (147 words)

The fluidics of our flow cytometer is represented in Fig. 1.**b**. Particles are constrained in the interrogation zone in the optofluidic flow cell through hydrodynamic focusing of the sample suspension with a sheath fluid. A flow controller (ElveFlow, OB1 MK3+) adjusts respective flow rates of sample and sheath through

regulating air pressure in pressurized liquid reservoirs. Flow rates are kept constant through closed-loop, PID-optimized feedback loops based on signals provided from a sample flow sensor (ElveFlow, MFS3. Range: 0 to ± 80 µL/min) and a sheath flow sensor (ElveFlow, MFS5. Range: 0 to ± 5000 µL/min). Samples are loaded by syringe into a 100 µL sample coil through a 6-port rotary valve (IDEX, V-451), which can alternate between load and inject states, where the sample coil alternates between being coupled to 1) the injection port and waste port or 2) sample pressure reservoir and flow cell, respectively.

2.2.3 Electronics Setup (147 words)

An overview of the electronics used for device control and data acquisition is shown in Fig. 1c. A radio-frequency driver (AA Opto-Electronic, MPDS1C2X-B45-0-95.125-RS) generates the RF control signals that are then amplified by an RF power amplifier (AA Opto-Electronic, AMPA-B-36-20.400) before being supplied to the individual AOFS. An analog output card (NI, PXIe-6711) provides analog control signals between 0–5 V DC to selectively operate the optical shutter controllers (Thorlabs, SC10). Signals from the SiPM are digitized by a field programmable gate array (FPGA; NI, PXIe-5764) at 1 GHz with 16-bit depth down-sampled in the FPGA by a factor of 2 to reduce the data stream. The recorded signals are relayed to the host computer using a producer-consumer architecture and subsequently saved locally for offline post-processing. A custom LabVIEW program (NI, LabVIEW 2022 Q3) was developed and run on the host computer to handle both instrument control and data acquisition.

2.2.3 Signal processing and data analysis (114 words)

Analysis and characterization of the recorded time series were performed using a custom offline routine developed in MATLAB (MathWorks, MATLAB R2022B) and is described in section 3.1 and illustrated in **Supplementary Fig. 2.3** for dual-beam experiments. For single-beam experiments we smoothed the recorded signal with a moving average Gaussian-weighted filter of 500 samples in window length. Next, we performed a variance-based gating method at 1-µs intervals, identifying peaks exceeding a threshold of 65.6 A.U. as potential events, and flagging events within 5 µs as potential coincident detections. The applied threshold value yielded < 200 events/second. For analysis of each event, we extract the peak intensity and FWHM for each event using the smoothed signal.

2.3 Flow cytometry analysis (228 words)

The 355 nm laser was operated at 50 mW output power in the dual-beam configuration and 100 mW in the single-beam configuration to keep total laser power consistent in the interrogation zone between experiments. Each AOFS was driven by a monotonic 33 dBm RF signal and configured to yield identical first-order diffraction power achieved through rotation of the HWP and confirmed using a laser power meter (Thorlabs, S130VC). The SiPM was supplied with a DC bias of 40 V. Sheath flow was kept constant at 3000 µL/min and sample flow at 2 µL/min (**Supplementary Fig. 2.5**) yielding a sample core of 6 µm and a particle transition time of 10.9 µs. Due to the rotation of the flow cell (Fig. 1a, **inset**), particles traversing the interrogation zone induce a small lateral movement relative to the scrolling motion that results in a slight Doppler shift in observed signal frequencies that allow for filtering out signals from optical interfaces. 40 measurements of 1 second duration each were recorded for each sample yielding

a total sample volume of 1.33 µl. A detection threshold was established using MilliQ water yielding < 100 events/second. 10-fold serial dilution control samples were analyzed to determine the optimal particle concentration range and limit coincident/swarm detection (**Supplementary Fig. 3.4**). All samples were diluted to a particle concentration of ≈ 2.5×10^4 particles/µl, which was within this range.

2.4 Lorenz-Mie Theory (151 words)

We model predicted scattered light intensity from particles traversing the scrolling interference using Lorenz-Mie theory. Equations are provided in Supplementary Material 1.1–1.7 [26, 27]. To describe scattering from an inhomogeneous light field we apply the superposition of individual homogeneous light fields [27–29]. Simulations were carried out for particles suspended in water (n_{med} = 1.343), for varying particle sizes ranging from 50 to 400 nm in diameter of both Au (n_p = 1.683 + 1.885i) [30] and PS (n_p = 1.636 + 0.008i) [31]. We assume that all particles are spherical with a homogeneous refractive index, the refractive index of the medium is uniform throughout the volume (either non-absorbing or absorbing), and each incident beam is considered a monochromatic plane wave at 355 nm wavelength [27, 32]. The simulated solid collection angles for determining the scattered light intensity were matched to the optical configuration of the instrument (angle = 0°; NA = 0.33).

3. Results

3.1 Operation of the flow cytometer

The near-counterpropagating laser beams (γ = 85°) result in a standing wave with a spatial wavelength of ≈ 133 nm in water (n = 1.343) [28, 33]. A central feature of the system is the precise 10 MHz scrolling frequency of the standing wave field, achieved by the relative frequency modulation of the two beams that results in a constant phase shift of the standing pattern. As particles traverse this light field, they are alternately exposed to regions of constructive and destructive interference as the standing wave is scrolled across their trajectories. Consequently, the scattered light intensity oscillates at the scrolling frequency of the interference pattern, acting as a carrier frequency that enables frequency lock-in detection of scatterers in the interrogation zone. This approach simultaneously suppresses broadband noise, offering improved signal-to-noise ratio. The scrolling frequency is well below the digitizer's Nyquist limit, ensuring high-resolution sampling of the oscillatory scattered intensity. For light-particle interaction, we employ a hydrodynamically focused stream to probe individual particles (Fig. 1a, **inset)**. At specific flow rates (sheath: 3000 µl/min, sample: 2 µl/min), we estimate a fluid velocity of ≈ 1.6 m/s within a ≈ 6 µm flow core [34].

Combining the scrolling interference pattern with hydrodynamically focused particles results in a frequency separation between static and dynamic scatterers. In fact, it is expected that the frequency of the oscillating signal for static scatterers equals the scrolling frequency (10Mhz). Scattering particles that move in a direction perfectly perpendicularly with the scrolling direction (z in our set-up) are also expected to produce a signal oscillating at 10MHz. However, scatterers moving at an angle from the z-

axis produce a signal that oscillates at a frequency slightly offset from the scrolling frequency. Specifically, a flow direction slightly tilted compared to the pattern induces a Doppler shift of the scattered signal, resulting in up- or down shifted frequencies for the intensity oscillations centered around the scrolling frequency. The magnitude of the motion-induced frequency shift is influenced by the particle's velocity and trajectory angle. This small motion-induced frequency shift enables discrimination between static and dynamic scatterers, e.g., from interfaces between the quartz flow cell and sheath fluid and particles in the sample (**Supplementary Fig. 2.1**). This was confirmed by a narrow 10 MHz peak from static scatterers and a broader ~ 9.4 MHz peak from particles. By switching the frequencies driving the two AOFS, we flip the scrolling direction of the interference pattern. This results in a sign-flip of the motion-induced 0.6 MHz frequency shift, effectively moving the observation frequency from 9.4 MHz to 10.6 MHz. Here, we use down-shifted signals, corresponding to a small lateral particle velocity in the scrolling direction (see **Supplementary Fig. 2.1c**).

We developed a custom offline routine for analysis of the recorded time series. In dual-beam experiments, frequency analysis showed particle signals at 9.4 ± 0.1 MHz and static scatterers at 10 MHz. Digitized signals were processed with a 4217-order equiripple bandpass filter designed via the Parks–McClellan algorithm, with a 9.3–9.5 MHz passband and 0.3 MHz transition bands, sampled at 500 MHz. Event detection was applied to the filtered signal at 1-µs intervals using variance-based gating, detecting peaks > 3 A.U (background signal is centered around 0 ± 2, see **Supplementary Fig. 3.2**). Peaks within 5 µs of other peaks were flagged as coincident and excluded from analysis. Event-level features were extracted from both raw and filtered signals. Mean intensity was extracted from raw signals within a 10 µs window per event, while oscillation amplitude, peak intensity, and full width at half maximum (FWHM) were obtained from filtered signals. Particle events were further identified by thresholding at peak ≥ 3 A.U. (**Supplementary Fig. 3.3**) and FWHM ≥ 2 µs.

3.2 Lower detection limit in dual-beam operation compared to single-beam operation

To assess instrument performance, we analyze Au and PS particles of varying sizes using the dual-beam configuration and compare the results to measurements using a single incident beam. By blocking one beam, our optical configuration allows for direct switching between both modes, enabling the instrument to operate in a side-scatter geometry.

Using the dual-beam configuration, we detect single-particle events across a wide range of sizes and materials, shown in Fig. 2. Event distributions are shown as 2D heat maps of signal offset versus amplitude, with marginal histograms illustrating the underlying distributions and a dashed magenta line indicating the most frequent event. For comparison, blank measurements of ultrapure water and PBS are shown in **Supplementary Fig. 3.1**. Although the smallest particle distributions overlapped substantially with background, the instrument can detect particles down to 15 nm Au and 100 nm PS based on both the shape and the particle count in these distributions (**Supplementary Fig. 3.5**). Overall, this feature-

based approach enables robust identification of true oscillatory events while suppressing noise-induced artifacts.

In contrast, the single-beam configuration could not resolve particles smaller than 70 nm Au and 152 nm PS from background (Fig. 3). Au particles between 125–200 nm also showed substantial distribution overlap, limiting size discrimination. In the dual-beam configuration, these particles were clearly resolved based on signal offset and amplitude. These results demonstrate that frequency-encoded illumination enhances signal-to-noise ratio and size resolution through selective processing of frequency-encoded scattering signals.

3.3 High-throughput detection of sub-micron particles

To quantify instrument throughput, 125 nm Au particles were measured at varying concentrations (**Supplementary Fig. 3.4a & b**). Here we found even at the highest concentration ≈ 6.65×10^5 particles/µl, particles were detected at 750 particles/s after excluding coincident events via signal processing. This remained within the linear regime of particle count versus reciprocal dilution, while average scattering signals stayed constant, ruling out swarm detection and indicating potential for higher throughput.

3.4 Understanding practical measurements through 3D Mie-scatter modelling

To validate our measurements, detected intensities were compared with Lorenz–Mie predictions (Fig. 4). The measured signal offset and amplitude for each particle species are shown as black dotted lines and red markers with whiskers, while the predicted values are indicated by a solid black line and red shaded region. Measured quantities are retrieved from magenta-colored lines illustrated in Fig. 2. The measurements agree well with the model for both Au and PS particles. Notably, the scattered intensity does not scale monotonously with particle size. Overall, the model accurately describes single-particle scattering in the inhomogeneous light field under our system conditions.

4. Discussion and outlook

We report the first implementation of FCM using a scrolling interference pattern to illuminate single particles, achieving detection limits of 15 nm (Au) and 100 nm (PS) with our current implementation. This approach overcomes key limitations of conventional FCM for submicron particle characterization. Compared to high-resolution FCM, our method effectively discriminates aggregates, differentiates particles by refractive index, and resolves populations within narrow size bands. The scrolling interference pattern provides improved SNR and resolution relative to single-beam illumination, as confirmed by direct comparison of instrument modes. Additionally, our instrument achieves event rates up to fivefold higher than previous nanoparticle-optimized flow cytometers [22]. While traditional high-resolution FCM systems use a focused light source to minimize out-of-focus excitation, we employ collimated light in both the single- and dual beam configuration. As a result, direct comparison to

existing systems is challenging due to differences in illumination geometry, though direct comparison of the system's two illumination modes. The dual-beam configuration provides a high-throughput methodology for nanoparticle characterization superior to NTA, as it remains effective across multiple particle species within a single sample and readily distinguishes particles by refractive index and size. Consequently, we propose our approach as a unified practical solution for submicron characterization, potentially replacing the need for multiple complementary measurements such as DLS, NTA, and TEM.

While our proof-of-concept instrument's capabilities have been demonstrated, its current configuration faces multiple limitations. A key limitation is the excitation source, as we selected a wavelength that maximizes the scattering cross-section for small particles while minimizing water absorption. However, this choice restricts the system to using a low NA detection lens, resulting in reduced light collection given in a specific direction. Overcoming these limitations and improving the system's performance we suggest two different approaches.

First, the limited light collected from the side-scatter cross-section is more sensitive to small particles, as larger particles primarily scatter light forwards and backwards. To increase sensitivity to larger particles without replacing the excitation source, a second detection system could be placed at a 45° angle relative to the existing lens. Assuming an identical detection system is positioned in this new orientation, we simulated the expected scattering intensity for Au and PS particles of various sizes (Fig. 5a **& b, panel (I)**). Adding the second detection angle would increase the resolution in discriminating primarily larger particles or different refractive indices, when comparing Fig. 4 **and panel (I) in** Fig. 5a-b. Unlike conventional FCM, our use of near-counterpropagating beams prevents us from placing a detector in the forward direction, as it would block one of the beams. Using this approach, we may improve the system without affecting the scattering cross section.

Second, using a 405 nm excitation source enables the use of high-NA optics with only minimal reduction in the scattering cross-section. To demonstrate this, we simulated our current configuration with varying excitation wavelengths (Fig. 5a-b, **panel (II)**). Compared to the expected scattering in Fig. 4, we observe a slight decrease in intensity, which reduces sensitivity for smaller particles. To compensate for this, a high-NA objective lens (NA = 1) can be applied to increase the collection angle. The effect of combining this high-NA lens with a 405 nm source is illustrated in Fig. 5a-b, **panel (III)**, where the signal's oscillatory behavior clearly differentiates between Au and PS particles. Furthermore, optics in this regime are more cost-effective. Consequently, we believe future implementations should focus on visible-spectrum excitation, ideally at shorter wavelengths.

While we present the first prototype of this FCM platform, there are multiple directions to enhance it. The core strengths of this platform are that it provides label-free discrimination of submicron particles in a high throughput manner demonstrated with sub-micrometer sized synthetic beads. Given that our optical design aligns with Phase-Doppler Anemometry (PDA) configurations, we may leverage established systematic approaches that could address current limitations in measurement specificity [35, 36]. This is also applicable for FCM, where a natural systemic improvement involves one or more fluorescent

channels. In summary, our newly developed FCM platform provides the first stepping stone in label-free size and refractive index characterization of submicron particles in a high-throughput configuration.

5. Conclusions

This work presents a label-free FCM platform for submicron particle characterization using scrolling interference pattern illumination. Based on high-throughput measurements of well-defined spherical particles, we demonstrate detection limits down to 15 nm for Au and 100 nm for PS at rates up to 750 particles/s. The observed scattering intensities align with Lorenz-Mie predictions for inhomogeneous light fields. In summary, this method offers a high-throughput, high-sensitivity, and label-free solution for submicron particle analysis.

Declarations

7. Funding Declaration

This work is supported by a New Exploratory Research and Discovery (NERD) grant from the Novo Nordisk Foundation (NNF20OC0059893), a Lundbeck Experiment grant from the Lundbeck Foundation (R346-2020-1257), a grant from H.C. Ørsted Foundation, and a grant from the DTU Skylab Discovery innovation program.

8. Author contributions

E.B.K. and J.B. conceptualized and supervised the project. – C.E.S.K. and J.P.R., developed and conducted the simulations. – C.E.S.K and L.P.A. implemented the instrument. – C.E.S.K, J.B., and R.M. designed the experiments – C.E.S.K and J.B carried out experiments and analyzed data with help from R.M., J.P.R., L.P.A., and E.B.K. - C.E.S.K. and J.B. drafted the manuscript, and all authors contributed to its completion.

9. Conflicts of interests

JB and EBK have applied for a patent regarding this instrument (EP application number 24163115.9). EBK is the inventor and owner of another patent related to this instrument (EP 4109076 A1). All other authors declare no conflicts of interest.

10. Supporting information

MATLAB scripts for evaluating the Lorenz-Mie coefficients and building an orthonormal basis from a 3d unit vector can both be found at https://people.compute.dtu.dk/jerf/code/.

11. Data availability

Data underlying the results presented in this paper are not publicly available at this time but may be obtained from the authors upon reasonable request.

References

1. Domingues, C. *et al.* Where Is Nano Today and Where Is It Headed? A Review of Nanomedicine and the Dilemma of Nanotoxicology. *ACS Nano* **16**, 9994–10041 (2022).
2. Bratovcic, A. Different Applications of Nanomaterials and Their Impact on the Environment. *International Journal of Material Science and Engineering* **5**, 1–7 (2019).
3. Gajanan, K. & Tijare, S. N. Applications of nanomaterials. *Mater. Today Proc.* **5**, 1093–1096 (2018).
4. Khot, L. R., Sankaran, S., Maja, J. M., Ehsani, R. & Schuster, E. W. Applications of nanomaterials in agricultural production and crop protection: A review. *Crop Protection* **35**, 64–70 (2012).
5. Joudeh, N. & Linke, D. Nanoparticle classification, physicochemical properties, characterization, and applications: a comprehensive review for biologists. *J. Nanobiotechnology* **20**, 262 (2022).
6. Zhang, C. *et al.* Progress, challenges, and future of nanomedicine. *Nano Today* **35**, 101008 (2020).
7. Yuana, Y., Sturk, A. & Nieuwland, R. Extracellular vesicles in physiological and pathological conditions. *Blood Rev.* **27**, 31–39 (2013).
8. Metselaar, J. M. & Lammers, T. Challenges in nanomedicine clinical translation. *Drug Deliv. Transl. Res.* **10**, 721–725 (2020).
9. Welsh, J. A. *et al.* Minimal information for studies of extracellular vesicles (MISEV2023): From basic to advanced approaches. *J. Extracell. Vesicles* **13**, (2024).
10. van der Pol, E. *et al.* Optical and non-optical methods for detection and characterization of microparticles and exosomes. *Journal of Thrombosis and Haemostasis* **8**, 2596–2607 (2010).
11. van der Pol, E. *et al.* Particle size distribution of exosomes and microvesicles determined by transmission electron microscopy, flow cytometry, nanoparticle tracking analysis, and resistive pulse sensing. *Journal of Thrombosis and Haemostasis* **12**, 1182–1192 (2014).
12. Hackley, V. A. & Clogston, J. D. Measuring the Hydrodynamic Size of Nanoparticles in Aqueous Media Using Batch-Mode Dynamic Light Scattering. in 35–52 (2011). doi:10.1007/978-1-60327-198-1_4.
13. Bachurski, D. *et al.* Extracellular vesicle measurements with nanoparticle tracking analysis – An accuracy and repeatability comparison between NanoSight NS300 and ZetaView. *J. Extracell. Vesicles* **8**, (2019).
14. Karow, A. R., Götzl, J. & Garidel, P. Resolving power of dynamic light scattering for protein and polystyrene nanoparticles. *Pharm. Dev. Technol.* **20**, 84–89 (2015).
15. Gardiner, C., Ferreira, Y. J., Dragovic, R. A., Redman, C. W. G. & Sargent, I. L. Extracellular vesicle sizing and enumeration by nanoparticle tracking analysis. *J. Extracell. Vesicles* **2**, (2013).
16. Hendrix, A. *et al.* Extracellular vesicle analysis. *Nature Reviews Methods Primers* **3**, 56 (2023).
17. Rikkert, L. G., Nieuwland, R., Terstappen, L. W. M. M. & Coumans, F. A. W. Quality of extracellular vesicle images by transmission electron microscopy is operator and protocol dependent. *J. Extracell. Vesicles* **8**, (2019).

18. Cossarizza, A. *et al.* Guidelines for the use of flow cytometry and cell sorting in immunological studies (second edition). *Eur. J. Immunol.* **49**, 1457–1973 (2019).
19. Arraud, N., Gounou, C., Turpin, D. & Brisson, A. R. Fluorescence triggering: A general strategy for enumerating and phenotyping extracellular vesicles by flow cytometry. *Cytometry Part A* **89**, 184–195 (2016).
20. McVey, M. J., Spring, C. M. & Kuebler, W. M. Improved resolution in extracellular vesicle populations using 405 instead of 488 nm side scatter. *J. Extracell. Vesicles* **7**, (2018).
21. Brittain, G. C. *et al.* A Novel Semiconductor-Based Flow Cytometer with Enhanced Light-Scatter Sensitivity for the Analysis of Biological Nanoparticles. *Sci. Rep.* **9**, 16039 (2019).
22. Zhu, S. *et al.* Light-Scattering Detection below the Level of Single Fluorescent Molecules for High-Resolution Characterization of Functional Nanoparticles. *ACS Nano* **8**, 10998–11006 (2014).
23. Steen, H. B. Flow cytometer for measurement of the light scattering of viral and other submicroscopic particles. *Cytometry Part A* **57A**, 94–99 (2004).
24. de Rond, L., Coumans, F. A. W., Nieuwland, R., van Leeuwen, T. G. & van der Pol, E. Deriving Extracellular Vesicle Size From Scatter Intensities Measured by Flow Cytometry. *Curr. Protoc. Cytom.* **86**, (2018).
25. de Rond, L. *et al.* A Systematic Approach to Improve Scatter Sensitivity of a Flow Cytometer for Detection of Extracellular Vesicles. *Cytometry Part A* **97**, 582–591 (2020).
26. Lorenz, L. Light propagation in and outside a sphere illuminated by plane waves of light. *The European Physical Journal H* **44**, 77–135 (2019).
27. Bohren, C. F. & Huffman, D. R. *Absorption and Scattering of Light by Small Particles*. (Wiley, 1998). doi:10.1002/9783527618156.
28. Jones, A. R. Light scattering by a sphere situated in an interference pattern, with relevance to fringe anemometry and particle sizing. *J. Phys. D Appl. Phys.* **7**, 310 (1974).
29. C R Negus & L E Drain. Mie calculations of the scattered light from a spherical particle traversing a fringe pattern produced by two intersecting laser beams. *J. Phys. D Appl. Phys.* **15**, 375–402 (1982).
30. Yakubovsky, D. I., Arsenin, A. V., Stebunov, Y. V., Fedyanin, D. Yu. & Volkov, V. S. Optical constants and structural properties of thin gold films. *Opt. Express* **25**, 25574 (2017).
31. Zhang, X., Qiu, J., Li, X., Zhao, J. & Liu, L. Complex refractive indices measurements of polymers in visible and near-infrared bands. *Appl. Opt.* **59**, 2337 (2020).
32. Frisvad, J. R., Christensen, N. J. & Jensen, H. W. Computing the scattering properties of participating media using Lorenz-Mie theory. *ACM Trans. Graph.* **26**, 60 (2007).
33. Hale, G. M. & Querry, M. R. Optical Constants of Water in the 200-nm to 200-μm Wavelength Region. *Appl. Opt.* **12**, 555 (1973).
34. Bruus, H. *Theoretical Microfluidics*. (Oxford University PressOxford, 1997). doi:10.1093/oso/9780199235087.001.0001.

35. Buchhave, P. & von Benzon, H. Exploring PDA Configurations. *Particle & Particle Systems Characterization* **13**, 68–78 (1996).
36. von Benzon, H. & Buchhave, P. The Phase-Doppler Method Applied to Very Small Particles. *Particle & Particle Systems Characterization* **11**, 55–62 (1994).

Figures

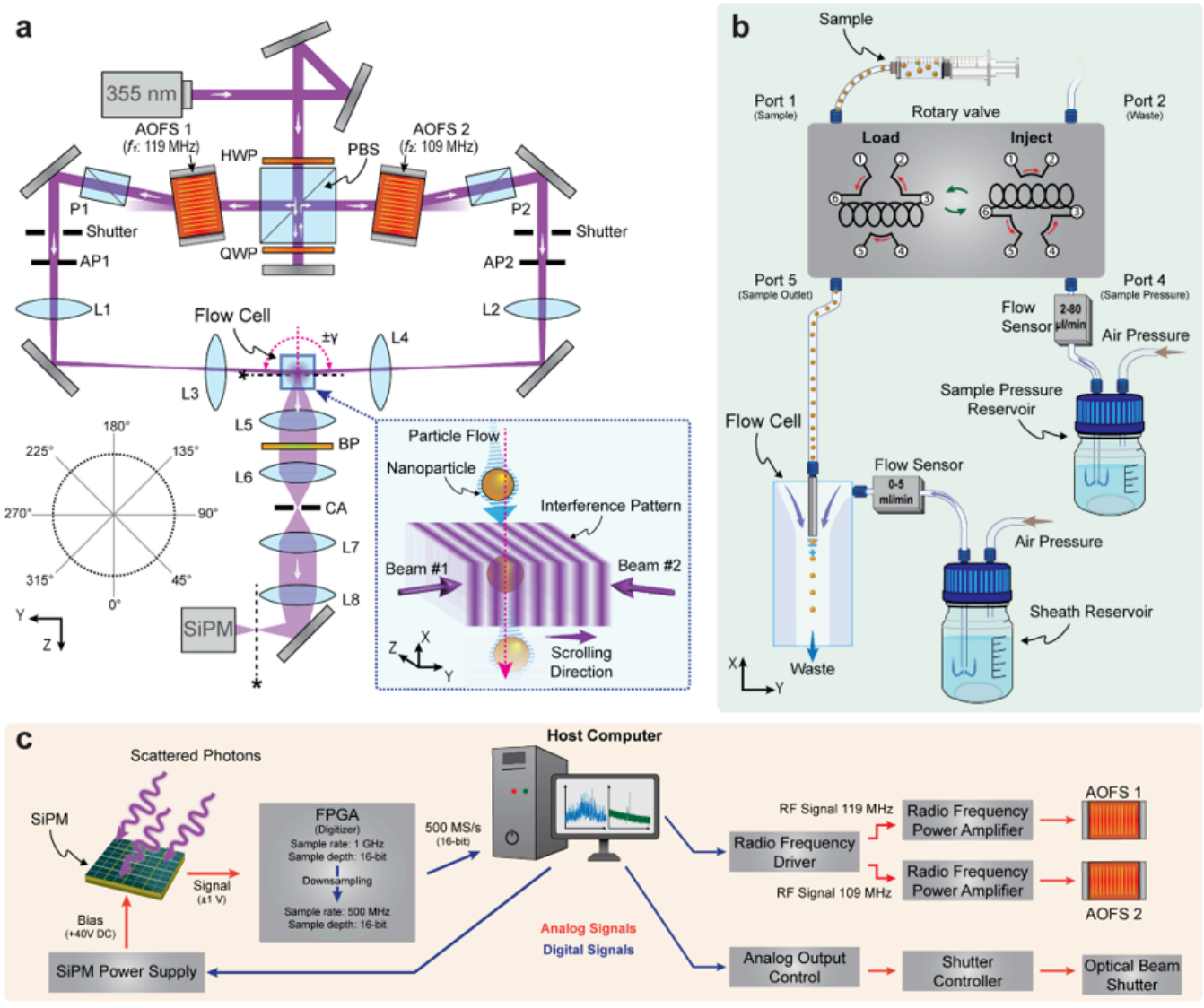


Figure 1

Schematic representation of the proposed flow cytometer; **(a)** Optical configuration for generating a continuous 10 MHz scrolling interference pattern and detecting scattered light from individual particles traversing a flow cell. A 355 nm CW-laser is split into two vertically polarized beams using a HWP and PBS. Each beam is frequency-shifted by an AOFS and projected into the flow cell. The two beams overlap in the interrogation zone, and the resulting scattered light from traversing particles is relayed through

two 4f systems, via a circular aperture conjugate to the interrogation zone, to a SiPM for intensity detection. **(b)** Microfluidic system for hydrodynamic focusing of individual particles in the interrogation zone. Samples are loaded into a coil and delivered to the flow cell via a rotary valve that switches between load and inject states. A pressurized reservoir supplies sheath fluid at 3000 μL/min, which combines with the sample fluid to align particles into a single file. **(c)** Electronic diagram and data flow. The host computer controls the AOFS frequencies and toggles optical shutters in the excitation path to illuminate the flow cell with either or both beams. Scattered photons are detected by a SiPM and digitized by an FPGA, which downsamples the signal to reduce the data rate. The resulting data stream is relayed to the host computer for offline processing.

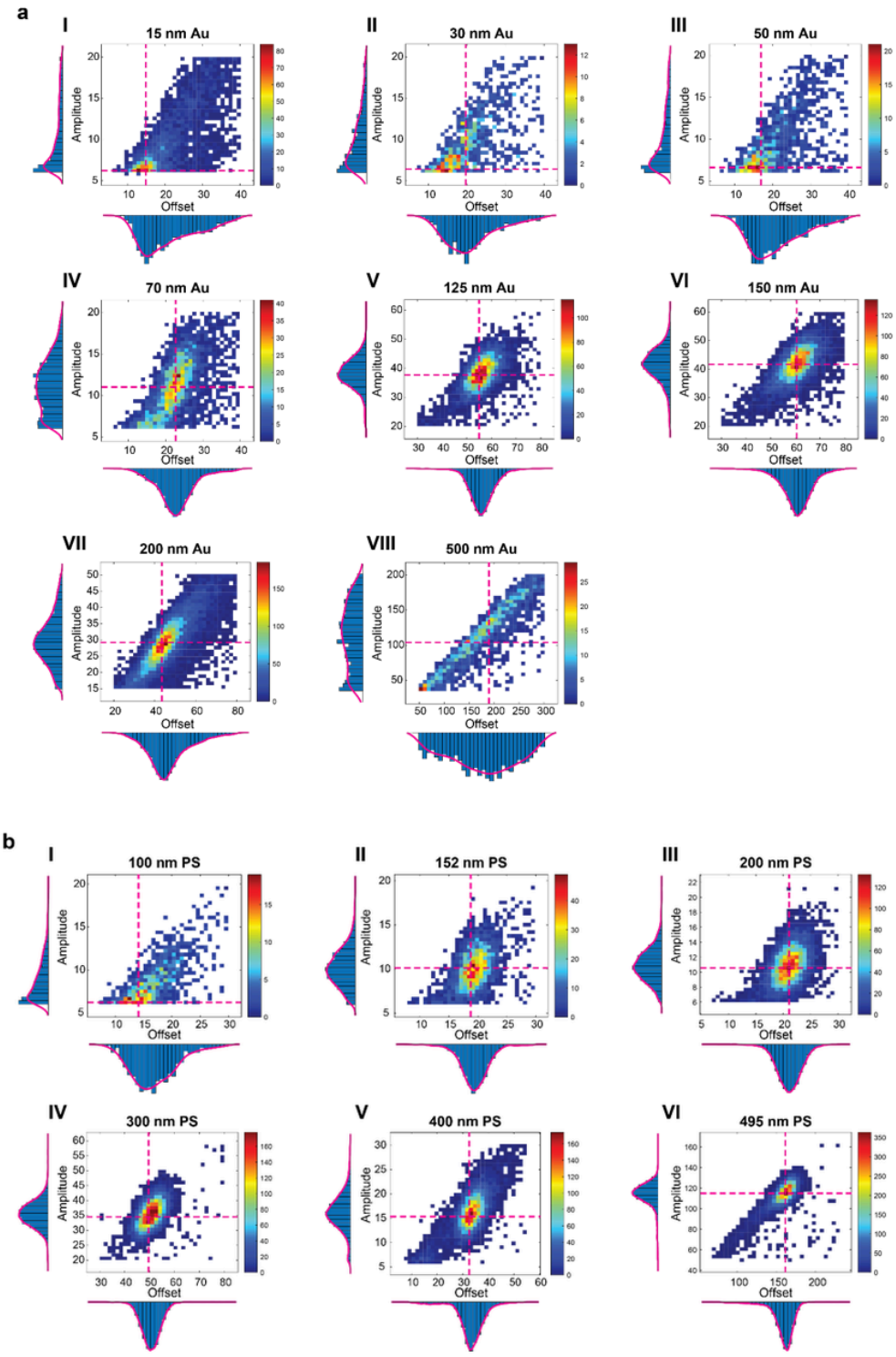


Figure 2

Single-particle event distributions for Au and PS species of various sizes under scrolling interference illumination**.** Each panel displays event distributions as 2D histograms based on signal offset (horizontal axis) and signal amplitude (vertical axis) where the number of observations is indicated with a color. In each panel heatmaps with corresponding color bars indicate observation frequency, while marginal histograms show the distribution of each parameter. A magenta kernel outlines the marginal distribution,

and dashed lines marking the respective peaks of the specific distribution. **(a)** Au particles ranging in size from 15 nm (I) to 500 nm (VII) in diameter. **(b)** PS particles ranging in size from 100 nm (I) to 495 nm (VI) in diameter.

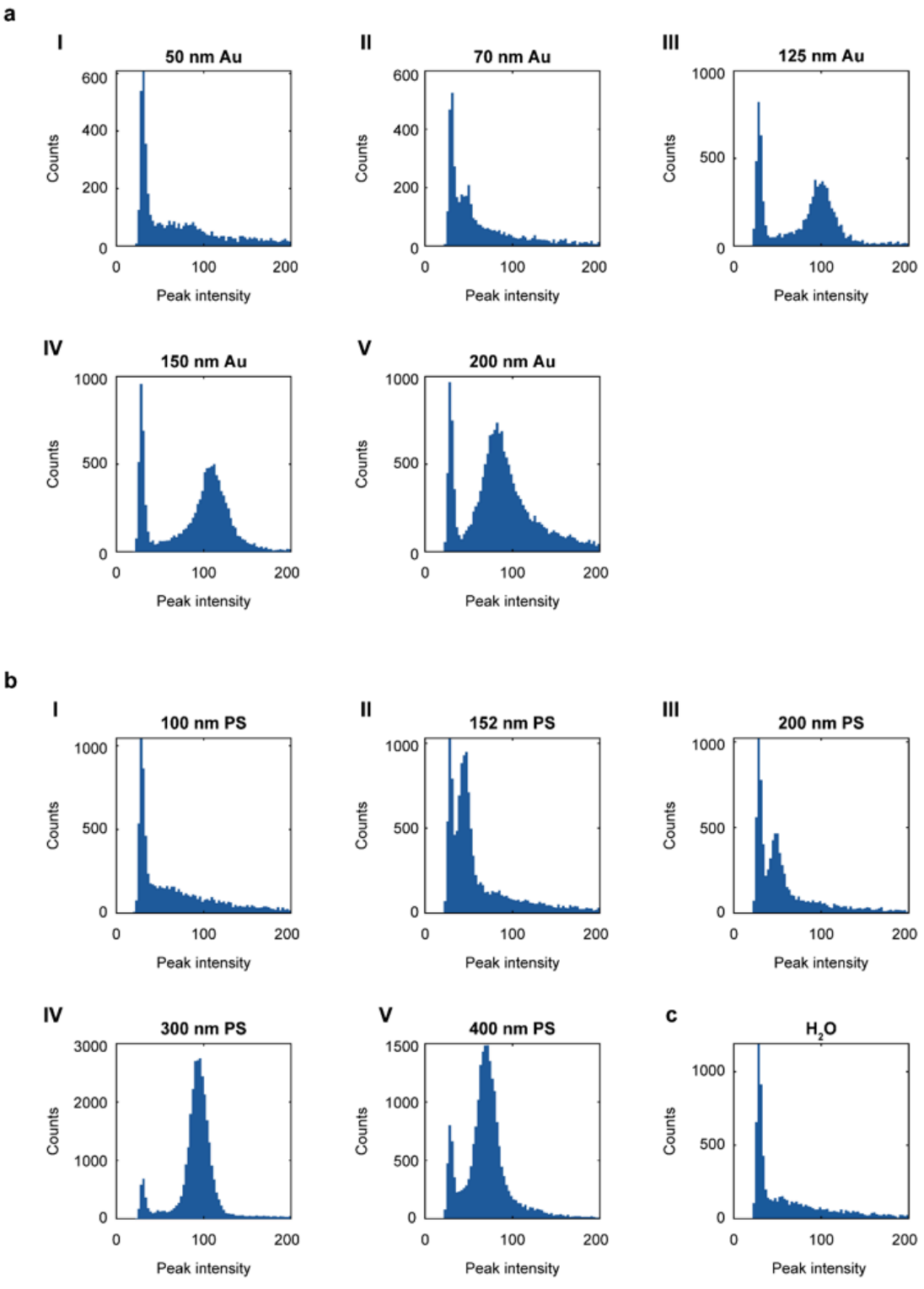


Figure 3

Peak intensity histograms for single-particle events of Au and PS particles of various sizes under single beam illumination. The background noise is visible as the prominent peak on the left-hand side of the distribution. **(a)** Au particles ranging in size from 50 nm (I) to 200 nm (V) in diameter. **(b)** PS particles ranging in size from 100 nm (I) to 400 nm (V) in diameter. **(c)** Peak intensity distribution for a blank sample (H_2O).

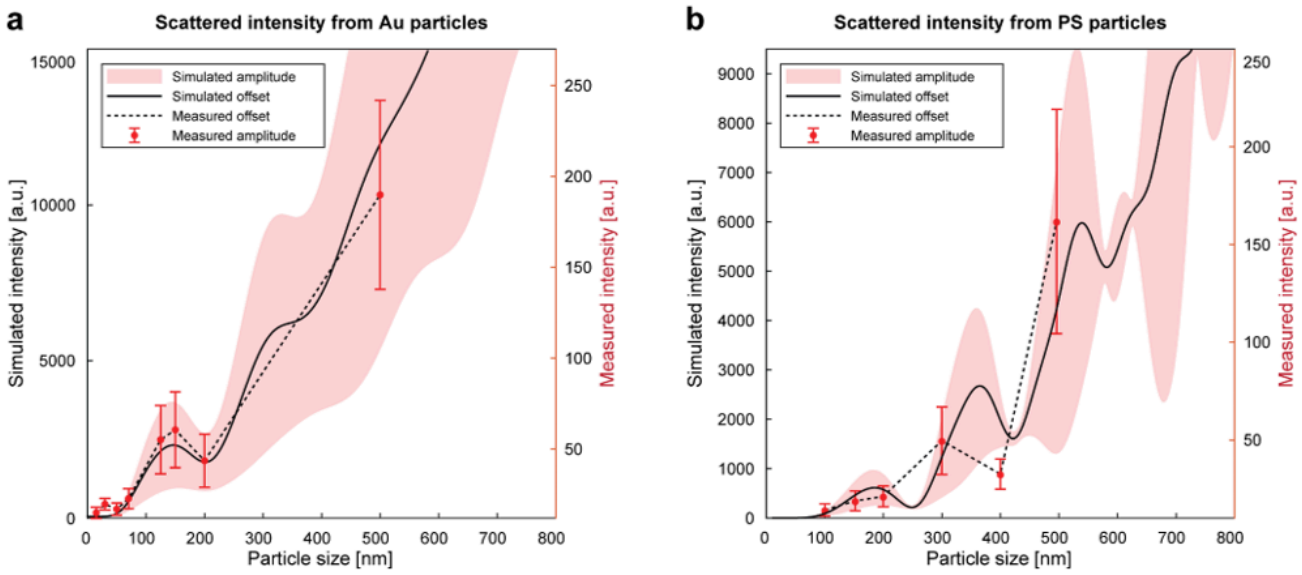


Figure 4

Comparison between simulated and measured scattered intensities for **(a)** Au and**(b)** PS particles**.** Expected intensities are shown for varying particle sizes within a scrolling, inhomogeneous light field. Light is collected in the side-scatter direction using a 0.33 NA lens. Theoretical oscillatory intensity signals are represented by a solid black line (simulated offset) and a red shaded area (simulated amplitude). Experimental measurements for distinct particle populations are indicated by black dotted lines (measured offset) and red whiskers (measured amplitude). The left-hand axis represents the simulated scattered intensities, and the right-hand axis represents the measured intensity.

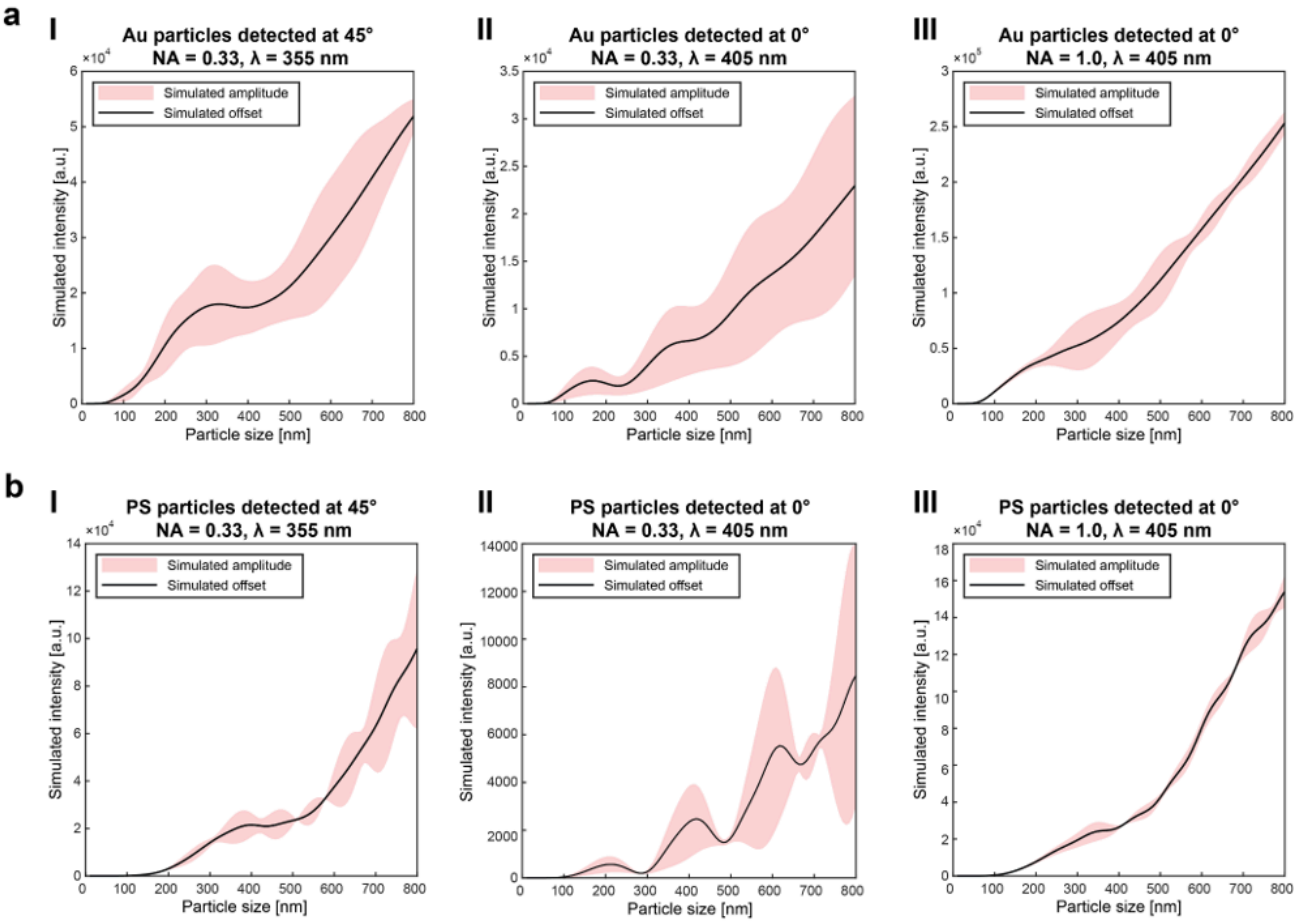


Figure 5

Simulations of alternative configurations for improved particle discrimination, focusing on additional collection angles and visible excitation with collection lenses of varying NA. Rows **(a)** for Au and **(b)** for PS particles each display three simulated optical alternatives: Panel (I) shows forward-scattered light collected by a 0.33 NA lens positioned at 45° relative to the current detection axis. Panel (II) depicts side-scattered light using a 405 nm excitation source with a 0.33 NA lens. Panel (III) represents the scattered intensity collected with a 1.0 NA lens in the side-scatter direction.

Supplementary Files

This is a list of supplementary files associated with this preprint. Click to download.

- SupplementaryMaterial.pdf